Homogeneous-resolution photoacoustic microscopy for ultrawide field-of-view neurovascular imaging in Alzheimer's disease

Ting Guo [a,b,c], Kedi Xiong [d,e,*], Bo Yuan [d,e], Zhenhui Zhang [d,e], Lijuan Wang [b,f], Yuhu Zhang [b,f], Changhong Liang [b,c,**], Zaiyi Liu [b,c,**]

[a] School of Medicine South China University of Technology, Guangzhou 510006, China
[b] Department of Radiology, Guangdong Provincial People's Hospital (Guangdong Academy of Medical Sciences), Southern Medical University, 510080, China
[c] Guangdong Provincial Key Laboratory of Artificial Intelligence in Medical Image Analysis and Application, Guangzhou 510080, China
[d] MOE Key Laboratory of Laser Life Science Institute of Laser Life Science, South China Normal University, Guangzhou 510631, China
[e] Guangdong Provincial Key Laboratory of Laser Life Science, College of Biophotonics, South China Normal University, Guangzhou 510631, China
[f] Guangzhou Key Laboratory of Diagnosis and Treatment for Neurodegenerative Diseases, Guangzhou 510080, China

ARTICLE INFO

ABSTRACT

Neurovascular imaging is essential for investigating neurodegenerative diseases. However, the existing neurovascular imaging technology suffers from a trade-off between a field of view (FOV) and resolution in the whole brain, resulting in an inhomogeneous resolution and lack of information. Here, homogeneous-resolution arched-scanning photoacoustic microscopy (AS-PAM), which has an ultrawide FOV to cover the entire mouse cerebral cortex, was developed. Imaging of the neurovasculature was performed with a homogenous resolution of 6.9 μm from the superior sagittal sinus to the middle cerebral artery and caudal rhinal vein in an FOV of 12×12 mm^2. Moreover, using AS-PAM, vascular features of the meninges and cortex were quantified in early Alzheimer's disease (AD) and wild-type (WT) mice. The results demonstrated high sensitivity to the pathological progression of AD on tortuosity and branch index. The high-fidelity imaging capability in large FOV enables AS-PAM to be a promising tool for precise brain neurovascular visualization and quantification.

1. Introduction

Brain imaging technologies capable of revealing the brain's physiological functions and activities in brain vasculature are indispensable tools for promoting Alzheimer's disease (AD) research [1,2]. AD is generally accompanied by damage to microvascular integrity and vascular alterations. Various regions of the cerebral cortex are functionally distinct yet interconnected [3,4]. These alterations in the vasculature of various brain regions are also contributing factors to early behavioral changes, that manifest as learning and memory deficits. The neurovasculature is responsible for supplying and metabolizing neural activity in the brain and is an essential component of brain homeostasis. Authoritative approaches, such as autopsy brain sections, have revealed the characteristic neuropathological markers and microvasculature through *ex vivo* labeling; however, these approaches do not offer the ability to monitor the process of vascular alterations in a long term [5,6].

Therefore, vascular imaging methods *in vivo* with high-resolution and a large field of view (FOV) are urgently needed to facilitate the understanding of the pathogenesis and process of chronic brain disease.

Methods for whole-brain imaging are developing rapidly. Magnetic resonance imaging (MRI), positron emission tomography (PET) and computed tomography (CT) can be used to perform volumetric brain imaging [7–10]. However, the spatial resolution of MRI is limited to several hundred microns and the temporal resolution is also restricted. PET and CT have the disadvantage of radiation exposure. In addition, optical techniques can obtain brain information with high spatial and temporal resolution [11,12], but due to the highly scattering nature of the skull and tissue, cranial windows must be opened or chemicals must be used to make the skull transparent, which may cause potential physiological changes and information loss.

Photoacoustic microscopy (PAM), which detects ultrasound signals of endogenous and exogenous contrasts induced by pulsed optical

---

absorption on a micro and macro level, has demonstrated an adequate ability to reveal pathological changes in tissue, such as vascular alterations in cancer patients and in patients undergoing inflammation treatment [13–16]. In previous reports, high-resolution photoacoustic microscopy [17,18], real-time photoacoustic microscopy [19,20] and wide-field photoacoustic microscopy [21,22] have all made great progress and have advanced the study of brain diseases to some extent. Conventional PAM systems utilizing planar or polygonal scanning, including galvo scanners [23,24], microelectromechanical system (MEMS) scanners [25,26], piezo scanners [27], voice coil motor (VCM) scanners [28], and polygon scanner systems [29], have made significant improvements in imaging speed, making it possible to capture more functional brain information. However, existing technologies are unable to accurately match the focal trajectory or closely follow the curvature of the mouse brain (especially the bilateral cerebral cortex), which leads to resolution deterioration and neurovascular information loss. Therefore, achieving high resolution and a large FOV simultaneously remains a persistent technical challenge. Optical microscopy with extended focal depth has been developed to resolve the out-of-focus problem caused by nonflat samples, and has achieved good results in high-resolution PAM. However, the Bessel beam [30,31] and synthetic aperture algorithm [32] have sidelobes, which affect the energy distribution and cause artifacts in the image. The needle-shaped beam method [33] has made breakthrough progress, but it may still be limited by the acoustic focal depth of the transducer, which may require compensation through algorithms. Contour scanning provides high accuracy and adaptability; however, the B-scan speed is limited due to the movement of the Z-axis motor [34,35]. Therefore, fast, effective, high-resolution neurovascular imaging with a large FOV for basic research in small animals remains a serious challenge.

Here, we propose arched-scanning PAM (AS-PAM) to image microvasculature from the central to bilateral cerebral cortex with homogeneous high-resolution. AS-PAM utilizes a strategy integrated with arched scanning to cover the entire mouse brain. The cantilever structure is lightweight and made of magnesium-lithium alloy providing high-speed scanning. This scanning strategy enables confocal laser excitation and ultrasound detection simultaneously, which achieves a high resolution of 6.9 μm. With brain imaging *in vivo*, it was demonstrated that the AS-PAM provides a larger effective FOV with high-resolution and has high adaptability to mouse brains at different periods than planar-scanning PAM (PS-PAM). In addition, we performed cerebral vascular imaging and quantified vascular parameters in AD and wild-type (WT) mice of different periods, demonstrating the laws of cerebral vascular alterations in AD and WT mice during the early stages. To the best of our knowledge, this is the first observation of vascular changes throughout the meninges and cortex during progression in AD and WT mice *in vivo*. With the unique advantage of capturing microvasculature distribution in a cambered brain surface, AS-PAM opens a new avenue for brain neurovascular research.

2. Materials and methods

2.1. Arched-scanning photoacoustic imaging system

The arched-scanning imaging concept of AS-PAM is schematically depicted in Fig. 1(a). The system's innovative scanning strategy provides a scanning trajectory that matches the mouse brain radian, enabling imaging with a greater FOV and consistent resolution. The arched-oscillating voice coil motor (AOVCM) is controlled by a driver and encoder to drive the cantilever, whose scanning trajectory forms a circular arc to cover the cerebral cortex in the mouse. As shown in Fig. 1(c), a soft ruler was bent into a circle with a radius. Utilizing an optimized
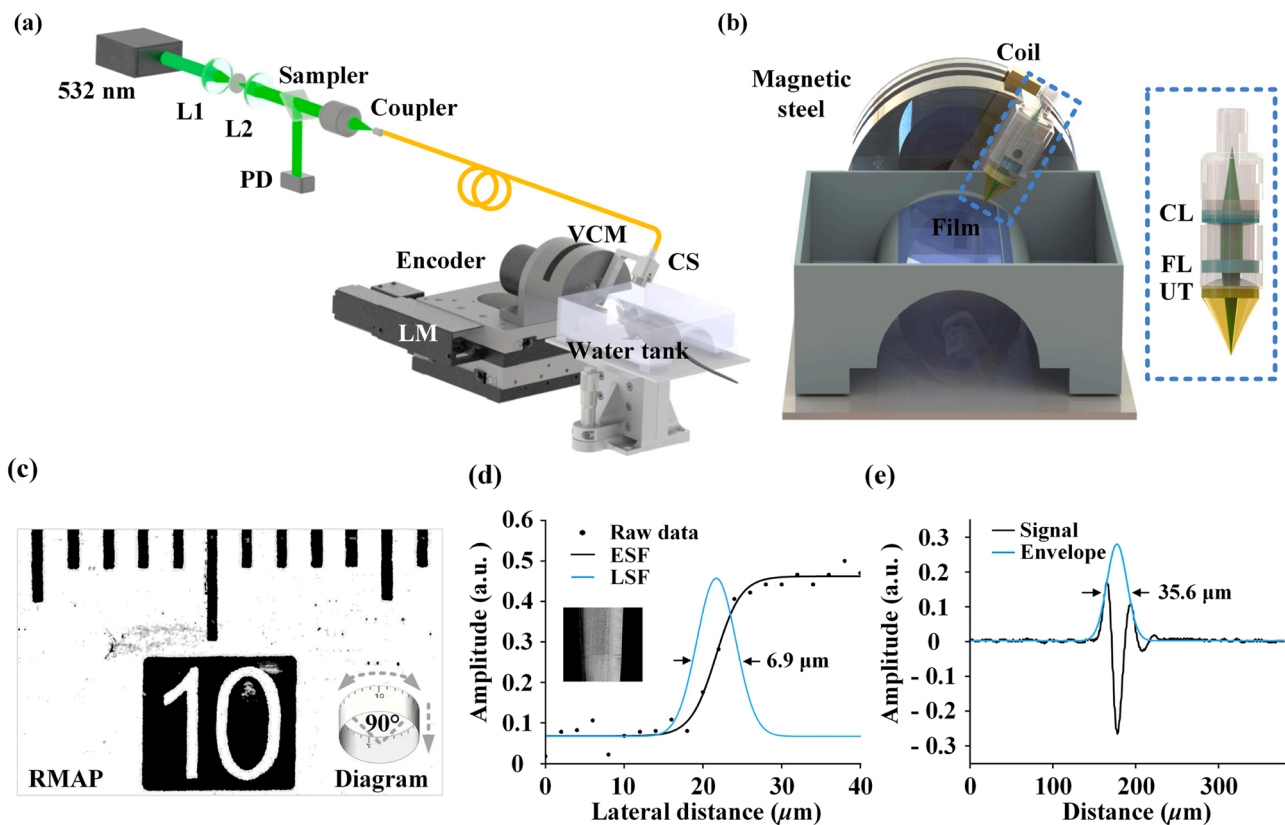
Fig. 1. AS-PAM system. (a) Schematic diagram of the system. VCM, voice coil motor; LM, linear motor; CS, cantilever structure; L1, lens 1; L2, lens 2; PD, photodiode. (b) Schematic diagram of the scanning and the close-up schematic of the optical path integrated into the cantilever structure. CL, collimating lens; FL, focus lens; UT, ultrasonic transducer. (c) FOV of the system and scanning angle. (d) Measured and fitted edge spread function (ESF) and derived line spread function (LSF). (e) Acoustic axial resolution.

cantilever structure, the imaging length was 12 mm at an oscillating speed of 10 Hz (Supplementary Movie 1) with a maximum scanning angle of 90°, which completely covered the entire adult mouse brain. The laser, acquisition card, AOVCM, and linear motor were triggered synchronously by a field programmable gate array (FPGA) module to achieve cross-section scanning and three-dimensional (3D) imaging. A pulsed laser (Innolas Photonics, mosquitooX-532–2-v) operating at 532 nm with a 12 ns pulse width was used as the excitation source. A photodiode was employed to monitor the energy fluctuation of pulsed lasers. The pulse repetition rate of the laser is 20 kHz. B-Scan speed is 10 Hz in mouse brain imaging and 5 Hz in the phantom experiment. In addition, a fixator suitable for the mouse brain was designed to place the mouse brain in the slot so that the height of the sagittal plane was relatively uniform.

Supplementary material related to this article can be found online at doi:10.1016/j.pacs.2023.100516.

2.2. Arched voice coil motor

The arched VCM consisted of a 180° semicircular magnetic steel stator (the central angle of the track is 90°) and a coil that moves along the arched track. The coil was connected to the moving shaft by a light rotating shaft. The AOVCM features high acceleration, hysteresis-free response and low noise, making it suitable for imaging systems with high spatial and temporal resolution. At the same time, the rotating shaft was connected to a 7 g cantilever structure made of aluminum magnesium alloy, which drives the cantilever structure to scan. The maximum torsional moment of the VCM used in this system was 0.17 N·m and the total stroke was 90°. The pulse width modulation signal output by FPGA was converted into a current signal in the motor driver to realize the motion acceleration and direction control of the VCM. The encoder with a resolution of 2000 is connected to the VCM for angle recognition and real-time feedback to the motion controller. The driver's closed-loop control circuit compensated for the error to realize accurate positioning.

2.3. Optical path system

The optical path output from the SMF was integrated into a small, lightweight cantilever structure (Fig. 1(b)). The laser beam was focused into a single-mode fiber (460 HP, Thorlabs) by a fiber coupler (PAF^{2}P–^{11}A, Thorlabs) and transmitted into a lightweight cantilever. The single pulse energy of the laser is 320 nJ and the maximal laser power was 6.4 mW. The laser beam was collimated through an aspherical lens, focused by an achromatic doublet lens, and finally illuminated the sample through the hollow of the PVDF-based focused ultrasonic transducer. To test the spatial resolution of the AS-PAM, a sharp edge of a blade was fixed and tangent to the circle of the focus scanning trajectory. The measured PA signal profile was calculated to obtain the edge spread function (ESF). After taking the derivative of the edge diffusion function, the line spread function (LSF) was obtained, and its full width at half maximum (FWHM) value was calculated. The AS-PAM achieved a 6.9 μm lateral resolution, as shown in Fig. 1(d) and (e). Fig. 1(e) presents the typical PA signal and Hilbert-transformed signal. The axial resolution was calculated to be 35.6 μm by measuring the FWHM of a Hilbert-transformed A-line. The theoretical acoustic focal depth was 340 μm.

2.4. Signal reception

The hollow of the PVDF-based focused ultrasonic transducer provided a main frequency of 35 MHz with a − 6 dB bandwidth of 115%. The PA signal was processed by an amplifier (LNA650, Rfbay), digitized at 250 MHz samples per second (M4i.4450-x8, Spectrum) and filtered by a digital bandpass filter. The image was reconstructed with a linear projection algorithm from polar to cartesian coordinates, which is similar to photoacoustic endoscopic imaging.

2.5. Scanning curve

The integrated structure of the optical path and transducer was screwed onto the cantilever structure (Fig. S2(c)). The radius of the curved is determined by the relative position of the integrated structure and the cantilever structure, and the relative position is changed by rotating thread. The adjustable length is designed to 4 mm. The curvature and FOV of imaging can be adjusted to suit different sizes of brain by varying the scanning radius and central angle. The radius and FOV corresponding to the length and angle are shown in Table 1. In addition, when the scanning radius is set to 10 mm, it can basically adapt to the brain surface in different mice. Mice from weeks 2–12 and months 4–10 were imaging with a defined parameter.

2.6. Linear Projection from polar to cartesian coordinates

The actual signal distribution obtained from polar coordinates scanning was projected into cartesian coordinates to achieve image reconstruction with bilinear interpolation, the coordinate transformation according to formula,

$$x = (L-l) * \cos(\frac{\pi - \theta}{2} + \frac{\theta \times n}{N}) \ , \ y = (L-l) * \sin(\frac{\pi - \theta}{2} + \frac{\theta \times n}{N}) \tag{1}$$

Where L is the distance between the central axis of the cantilever and the receiving surface of the transducer. l was the distance between the initial PA signal position and the receiving surface of the transducer, which is calculated using the position of the signal time series and the sampling rate of the acquisition card (Fig. S2(c)). θ was the maximum set swing angle. N was the total sampling number of A-line. n was the sequence number of the A-line. Finally, the missing pixels in coordinate transformation were obtained by bilinear interpolation. The 3D image (Fig. 3 (a)) was achieved by the software *Volview* by stacking the sequence number of B-scans.

2.7. Experimental preparation

"Female C57BL/6 mice were first anesthetized with 5% isoflurane in an oxygen/air mixture in an animal tank (200/800 ml min-1), after which mice were maintained in an anesthetized state with 1.0% isoflurane in an oxygen/air mixture (100/400 ml min-1) fixed in a fixator. Experimental mice were treated with hair removal and scalp removal only, leaving their skulls exposed. Next, the skull was treated with a saline swab to remove the fascia and keep it moist, without thinning and transparency. The ultrasonic gel was filled between the skull and a transparent polyethene film. During the experiment, mice were passed through a heating pad to maintain a constant body temperature. The mouse brains were attached to a custom-designed adjustable brain scaffold and fitted with a breathing mask. Female C57BL/6 mice (8 weeks old) were used for the experiment performed to validate the homogenous resolution and female C57BL/6 mice from weeks 2–12 were used for the experiment performed to evaluate the effective imaging FOV for different age groups. For the experiment of neurovascular development between AD model mice and WT, mice were evaluated at different periods, APP/PS1 double transgenic male mice were divided into four groups (number of AD mice n = 3 for all age groups), including 4, 6, 8 and 10 months-old animals as well as age-matched WT littermates (number of WT mice n = 3 for all age groups) of the same sexes. APP/PS1 mice expressing a chimeric mouse/human amyloid precursor

Table 1
Corresponding values of FOV and trajectory radian to scanning radius.

Radius (mm)	6	7	8	9	10
Imaging width (mm) (Pendulum angle 90°)	9.4	11.0	12.6	14.1	15.7
Trajectory curve (°) (Arched length 12 mm)	-	-	85.9	76.4	68.8
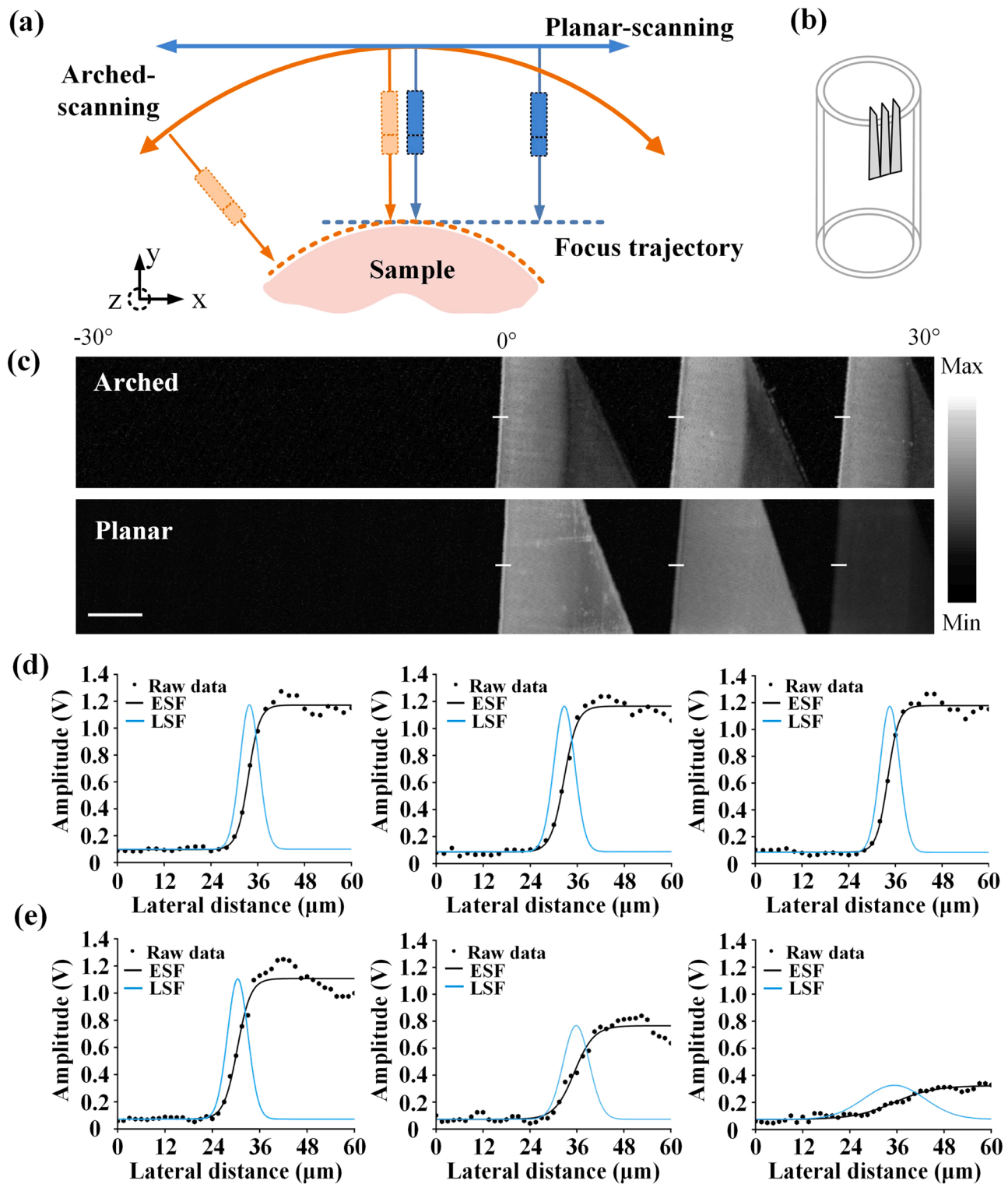
Fig. 2. Phantom imaging of arched scanning and planar scanning. (a) Schematic diagram of the focus trajectories. (b) Schematic diagram of blade arrangement. (c) The PA images of the blade. (d) Measured and fitted edge spread function (ESF) and derived line spread function (LSF) of arched-scanning imaging. (e) Measured and fitted edge spread function (ESF) and derived line spread function (LSF) of planar scanning. Scale bar in (c), 0.5 mm.

protein (Mo/HuAPP695swe) and a mutant human presenilin 1 (PS1-dE9), both directed to CNS neurons. Both mutations are associated with early-onset Alzheimer's disease. All animal procedures were reviewed and approved by the Medical Research Ethics Committee of Guangdong Provincial People's Hospital." We have added animal experimental preparation to Method 2.7.

2.8. Vascular parameter quantization

The raw data were processed by band-pass filtering to remove the noise signal and improve the SNR. The binary diagram of blood vessels was obtained by adaptive threshold segmentation image. Vascular density (*VD*) was defined as the ratio of the pixel value of the vascular
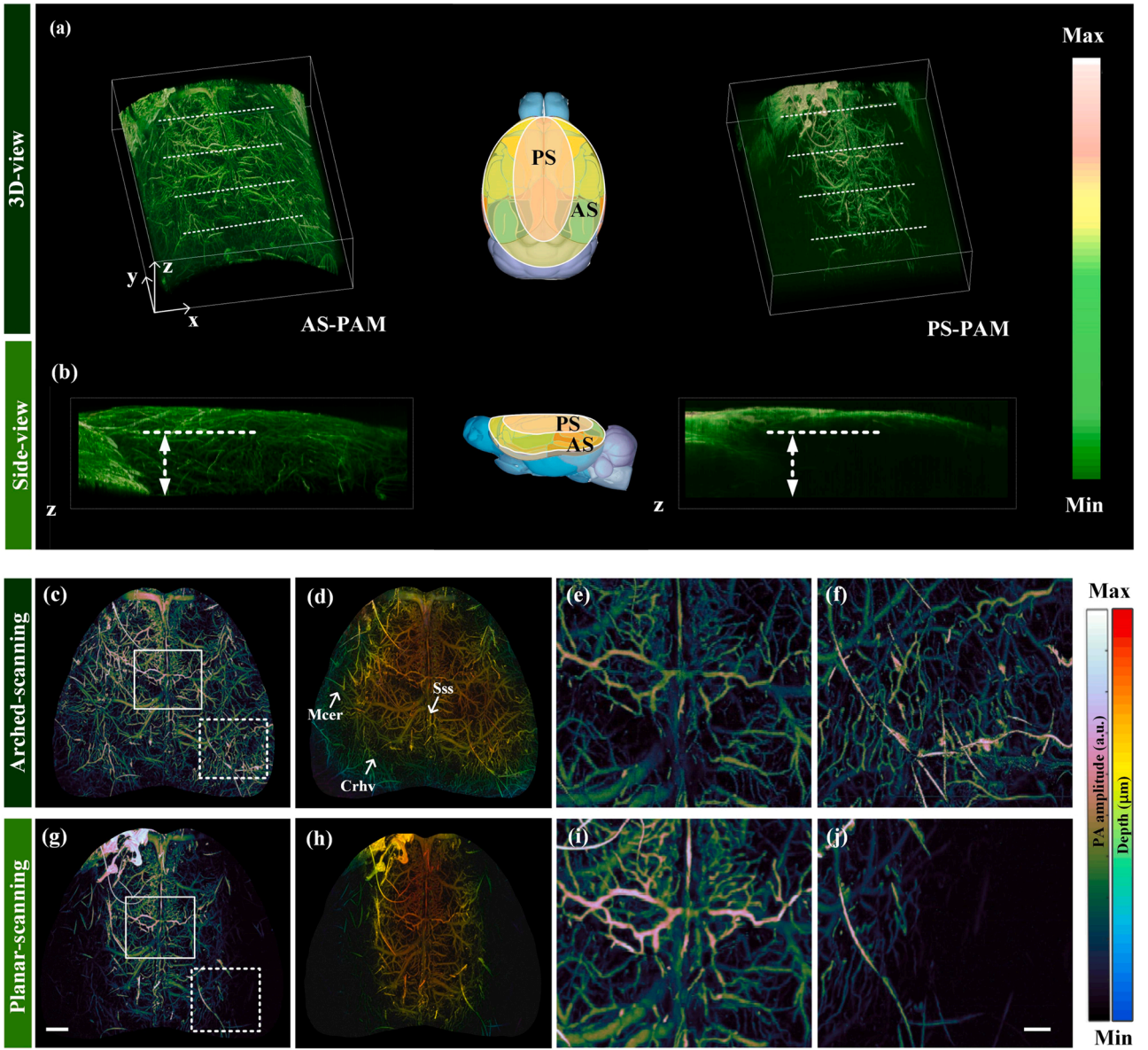
Fig. 3. Comparisons between arched-scanning imaging and planar-scanning imaging. (a) 3D image of mouse brain vasculature and the model map. (b) Side view of the 3D brain image in (a). (c) and (g) Maximum amplitude projection (MAP) from arched-scanning and planar-scanning. (d)and (h) The color-coded depth microvasculature image of the mouse brain vasculature over the entire cortex. Sss, superior sagittal sinus, Mcer, middle cerebral artery, Crhv, caudal rhinal vein [40]. (e) and (i) Close-up images of the solid box region in (c) and (g), showing the vascular details of the center area. (f) and (j) Close-up images of the dashed box region in (c) and (g), showing the vascular details of the lateral area. Scale bar in (g), 1 mm and scale bar in (j), 300 μm.

signal to the total pixel value [36].

$$VD = \frac{\sum_{i=1}^{m} \sum_{j=1}^{n} V(i,j)}{m*n} \quad (2)$$

where $V(i,j)$ is the vessel signal pixel on the binary image and $[m, n]$ is the size of the image (Fig. 4(c) and Fig. 6(h)). The vascular skeleton diagram was obtained through the binary image obtained by the above operation steps and the operation of retrograde morphology. Perfusion vessel density (*PVD*) was defined as the ratio of the pixel of the vascular skeleton to the pixel of the total skeleton.

$$PVD = \frac{\sum_{i=1}^{m} \sum_{j=1}^{n} P(i,j)}{m*n} \quad (3)$$

where $P(i,j)$ is the vessel signal pixel of centerline on the skeleton image

(Fig. 4(d)). The blood vessel edge is obtained by edge recognition of the binary image. The vascular centerline was used as a search clue, and Euclidean changes were made to the binary graph to calculate the shortest distance between the two edges of the vessel as the vessel diameter (*VD*). The branching index branch index was described as the number of vessel junctions normalized per unit area (Fig. 6(g)) and was analyzed using the Angio tool of ImageJ. The vessel tortuosity index (*VTI*), a commonly used measurement index of retinal curvature, was used to quantify the curvature of blood vessels (Fig. 6(i)).

$$VTI = \frac{0.1 SD_\theta.N.M.L_A}{L_C} \quad (4)$$

$$M = \frac{1}{Ip+2} \sum_{i=1}^{Ip+2} \frac{L_{Ai}}{L_{Ci}} \quad (5)$$

where SD_θ was the standard deviation of the angular differences
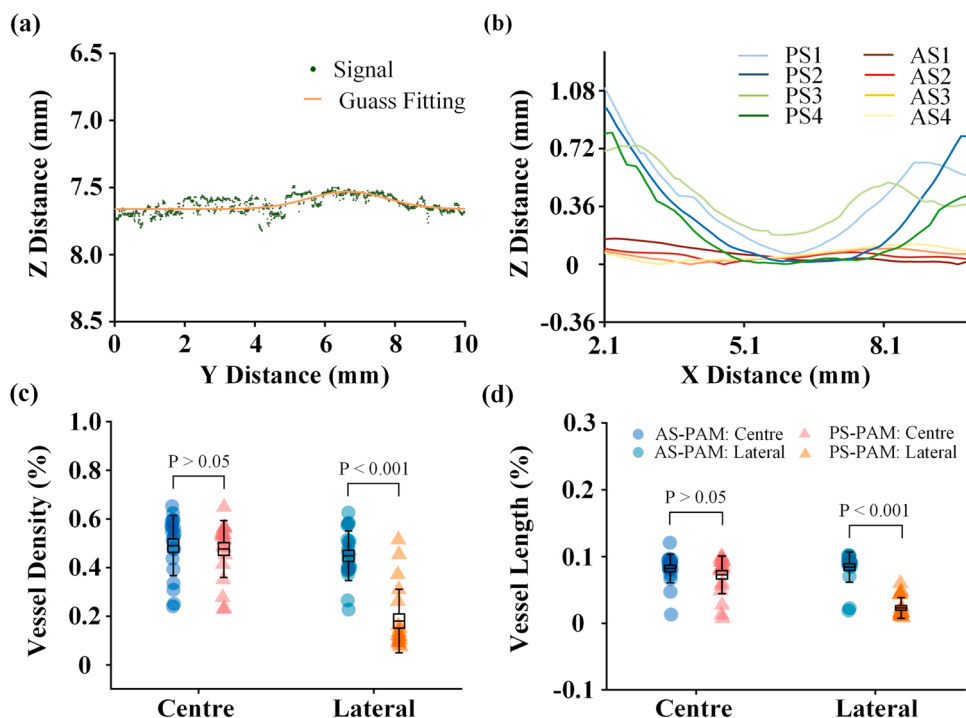
Fig. 4. Data analysis and quantification. (a) Elevation variation of the brain contour in the sagittal plane. (b) Focal deviation statistics of arched-scanning and planar-scanning at different positions. 1, 2, 3, and 4 correspond to Fig. 3(a). (c-d) Vessel density and vessel length of the central and lateral regions in the MAP of Fig. 3(c) and (f).
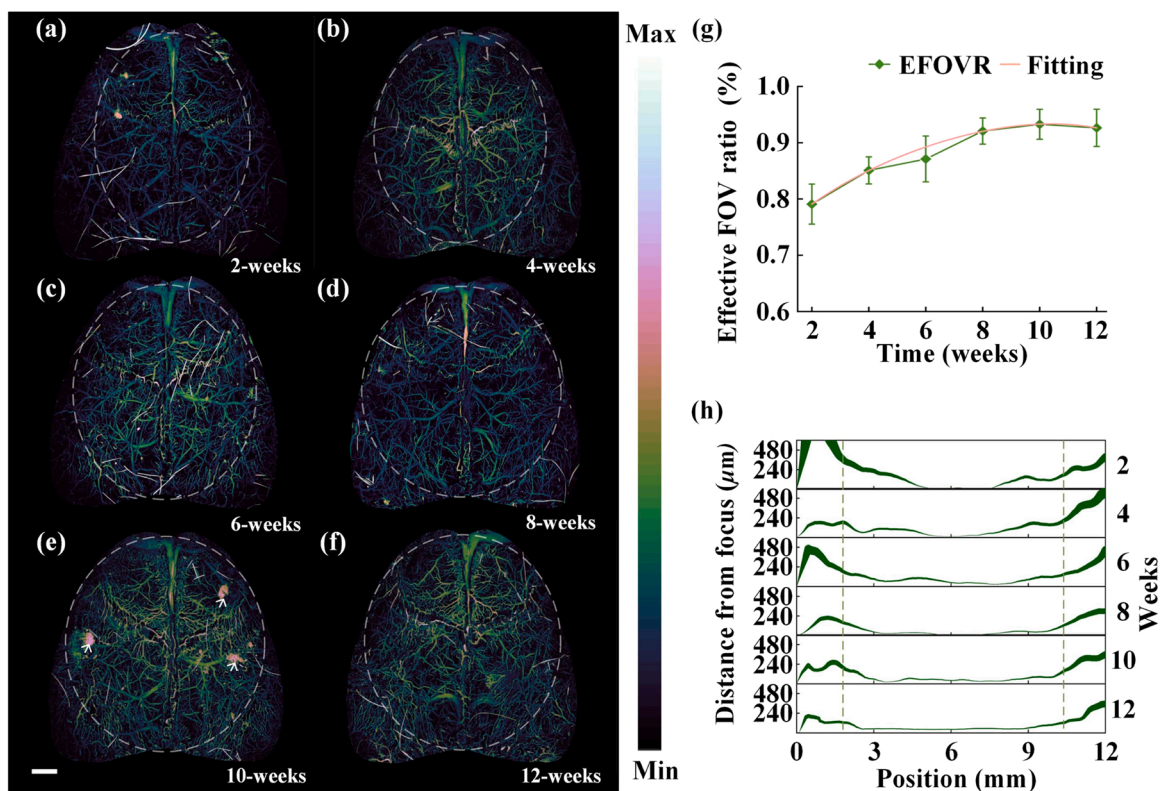
Fig. 5. AS-PAM brain imaging at different weeks of ages. (a-f) AS-PAM images of the mice's brains at weeks 2, 4, 6, 8, 10, and 12. (g) Effective area ratio for mouse brain imaging. (h) The distance of the signal position from the focus position in coronal brain images of mice at different weeks of age. Scale bar, 1 mm.

between each pixel of the centerline of skeleton and the lines tangent to the X-axis. N was the number of critical points where the first derivative of the centerline vanishes. M was the average ratio of the length of the centerline to the length of the chord between pairs of inflection points, including the end points of the centerline. Finally, L_A and L_C are the lengths of the centerline and its chord, respectively [37–39].
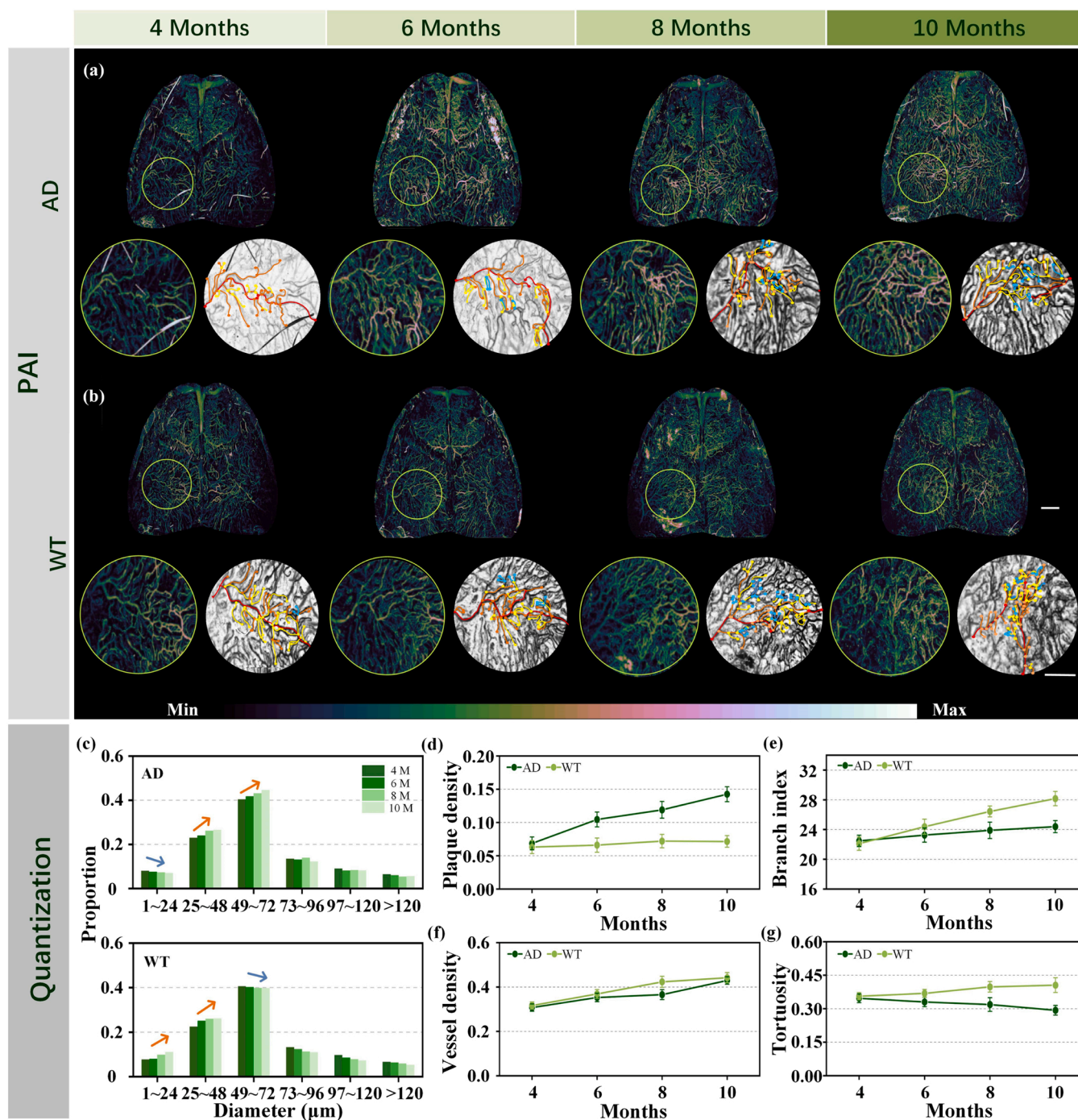
Fig. 6. Imaging and quantization of AD model mice and WT mice at different periods. (a, b) PA imaging and close-up images of AD model mice and WT mice. The numbers represent the sample number. (c) Statistics of the proportion of different vessel diameters in (a, b). (d-g) Comparison of plaque density, vessel density, branch index and tortuosity. AD, n = 3 for all age groups; WT, n = 3 for all age groups, Scale bar in (b), 1 mm.

3. Results

3.1. AS-PAM provides a more authentic measurement of a cambered surface than PS-PAM

The resolution homogeneity, effective FOV and authenticity in AS-PAM and PS-PAM were assessed by imaging three blades and a striped plastic sheet. In comparison to the focus trajectory of planer scanning, the focus trajectory of arched scanning is more matched to the radian of the sample, especially for the bilateral (Fig. 2(a)). Fig. 2(c) presents the imaging results of the blades. Schematic diagram of the sample as shown

in Fig. 2(b), blades arranged along the tangents of a circle with 8 mm radius. Obviously, the resolution and effective FOV of the planar scanning declined rapidly, the reason is caused by the combination of the decline in unit energy density of the light and in receiving efficiency, which was caused by the out-of-focus. The changes in signal-to-noise ratio (SNR) and effective FOV are more intuitive in striped plastic sheet imaging (Fig. S1). However, the imaging in arched scanning maintains homogeneous resolution and consistently high SNR in the entire FOV. To accurately quantify the differences in homogenous resolution and imaging authenticity, we analyzed the resolution at different depths. Fig. 2(d) shows the resolution of the arched scanning, which

remain homogenous within the radius variation of 60°, while the resolution and amplitude of the planar scanning deteriorate rapidly (Fig. 2 (e)). AS-PAM maintains homogeneous resolution and intensity over the entire FOV. The unique advantages of homogenous resolution and effective FOV enable AS-PAM achieve more accurate images, which improved the accuracy of global data quantification.

3.2. AS-PAM reveals the neurovasculature with high spatial resolution in a large FOV

The above experiments proved that AS-PAM is better able to homogenous resolution images of arched samples. We comparatively validated the coverage imaging ability of AS-PAM and PS-PAM for the whole meningeal and cortical regions *in vivo*, including the difference in effective FOV and spatial resolution homogeneity. Three-dimensional images are shown in Fig. 3(a). The PS-PAM image shows severe out-of-focus regions on both sides of the brain, resulting in reduced resolution and a reduced SNR. In contrast, the AS-PAM image maintains homogeneous imaging quality. In the side-view image, the height drop of the mouse brain was displayed more clearly from the sagittal suture in the cranial vault to the bilateral area and the loss of information in the lateral brain regions was more apparent in the planar-scanning images (Fig. 3(b)). The mouse brain model illustrates the difference in the effective FOV between the two scanning strategies [41]. The system combines three motors, which can independently perform arched scanning or planar scanning and can be repeatedly positioned. The optical path, focus position, and step distance are the same. The 3D AS-PAM images were reconstructed by the software *Volview* by stacking the sequence number of B-scans. Fig. 3(c) and (g) show the MAP of the data in Fig. 3(a). Under the same focal depth of the optical path, PS-PAM imaging could not obtain images of the whole brain. The depth coding images (Fig. 3(d) and (h)) showed that the brain contour had a small depth variation from the anterior fennel to the hermitic suture of the sagittal sinus (the mouse brain was placed at a certain angle so that the sagittal plane contour could maintain a relatively consistent height, and the calculation results are shown in Fig. 4(a)). However, there were significant changes in the brain contour of the coronal plane. Therefore, many brain imaging studies have focused on intermediate regions, ignoring the bilateral brain. We performed comparative imaging of the central region and bilateral brain regions between AS-PAM and PS-PAM, as shown in Fig. 3(e, f, i and j), which were taken from the box area in Fig. 3(c) and (g), respectively. They revealed that the resolution and effective imaging information are basically the same in the central region, while the resolution of the PS-PAM was reduced and the information was missing in the edge.

Using the linear projection algorithm and image segmentation, the adaptation degree of the AS-PAM system to neurovascular imaging was further quantified and the ability of bilateral cerebral microvascular information was characterized. Fig. 4(a) shows the alterations in the height of the mouse brain contours along the Y-direction. The height of the mouse brain contours in the sagittal plane could be kept relatively consistent by placing the mouse brain at a certain angle. The time series of signal points were transformed into spatial series, and the distance between the signal and the focus position was calculated (Fig. 4(b)). It can be observed that the deviation distance of arched scanning was within the Rayleigh length, while the signal at both sides of the planar scanning was out of focus seriously. Furthermore, a sliding window of 500×250 pixels was designed to analyze the vessel features on the central and lateral regions in the images of AS-PAM and PS-PAM. As shown in Fig. 4(c), there was a significant difference ($p < 0.001$) in the vessel density of the lateral region between the AS-PAM ($0.44\% \pm 0.01\%$) and PS-PAM ($0.18\% \pm 0.01\%$), which numerically verifies significant differences in the signal in the bilateral brain. The lateral region of the AS-PAM image ($0.08\% \pm 0.01\%$) also showed a significantly ($p < 0.001$) higher vessel length than the PS-PAM image ($0.02\% \pm 0.01\%$), indicating loss of vascular information in PS-PAM images

(Fig. 4(d)). The vessel density and length of the central region were weakly distinguished ($p = 0.898$, $p = 0.338$) between the AS-PAM (0.49%, 47%) and PS-PAM (0.08%, 0.07%), which might be flat in the middle brain region relatively. Among them, the reason for the deviation value is that there was a certain error in the hair around the eye during the blood vessel segmentation. It is noteworthy that the mean values of AS-PAM were similar in the central and bilateral regions in vessel density and vessel length. The quantified estimated results showed that AS-PAM had relatively better brain imaging ability than PS-PAM.

3.3. Quantitative evaluation of neurovascular monitoring in normal and AD model mice at different periods in vivo

The majority of neurodegenerative diseases are slow lesions and reflect different stages. Through our observation, the radian of the mouse skull is decreased to a certain extent during development. Mice are considered to be in the adult stage nine weeks after birth [42]. At this time, the skeletons of the mice are believed to be fully developed, and the overall brain shape has been determined. Fig. 5(a -f) show the MAP images of mice at different ages of weeks 2, 4, 6, 8, 10, and 12, underling the same standard. Meningeal and cortical blood vessels were clearly visible in the bilateral brains of mice of all ages. The three spots appearing (white arrow) in Fig. 5(e) are bleeding spots, resulting from individual differences. To accurately increase the coverage of mouse brain imaging, the fontanelle was located and 10 B-scans were extracted 6 mm away from the fontanelle. The effective FOV ratio was defined as the proportion of the width of the effective signal to the total width of the B-scan, as shown in Fig. 5(g). The effective FOV ratio of the system increased with the age of mice, but the effective imaging length ratio of mice remained stable after 8 weeks, and the effective coverage rate was more than 90%, which is shown in the dotted box in Fig. 5(a-f). In addition, the distance between the signal position and the actual focus position for each B-scan image in mice of different ages was calculated (Fig. 5(h)). The results showed that signal position and focus position have high overlap rates for images of mice of different periods. The imaging system can cover almost the whole brain and maintain relatively homogenous resolution during the whole growth and developmental period of mice.

In AD pathology, alterations in neurovascular function and morphology have been observed in electronic speculum due to the deposition of Aβ plaques covering the cortex and vessels [43]. Moreover, the exact area and location of neurovascular lesions in AD is uncertain and the regularity have not been validated *in vivo*. Imaging with a large FOV can observe comprehensive and global quantification, which is more accurate than local quantification. It has been proven that large-FOV imaging with homogenous resolution has advantages in terms of authenticity and quantification accuracy [34]. To further observe the comprehensive regularity of changes in neurovascular features at different stages of AD and in WT mice *in vivo*, neurovascular imaging and quantification were performed using the AS-PAM system on the genetically engineered mouse line APP/PS1 which has been proven to be useful in AD pathology research. Fig. 6(a) and (b) show the whole-brain meningeal and cortico-neurovascular imaging of AD mice and WT mice in the same litter at the ages of months 4, 6 8 and 10, respectively. The morphological features of the vessels in the lateral brain are evident in the scaled-up images. Moreover, the four levels of branching and nodes of the two main vessels in the central and lateral brain are marked with red, orange, yellow and blue lines for levels 1–4, respectively. While the branching features varied considerably, no clear regularity was observed. Therefore, the vascular parameters of the whole brain were quantified and analyzed further. The brain vessel density of both APP/PS1 mice and WT mice increased significantly with age and the quantification of vessel density is shown in Fig. 6(d). The proportion of blood vessels with different diameters was counted in Fig. 6(c), which shows the variation trend of blood vessel diameters in AD model mice and WT mice in different months. This finding reveals that the degree of

microangiogenesis in AD model mice is lower than that in WT mice. More importantly, the branching index of AD model mice was not significantly increased, while that of WT mice showed an increasing trend (Fig. 6(e)), and the tortuosity of the vasculature was also lower than that of WT mice, showing a decreasing trend (Fig. 6(g)). The branching index is a marker parameter that indicates the neo-vascularization of blood vessels [44]. In previous studies, the Aβ proteins attached around and deposited in the meningeal vessel walls and cortical interstitial spaces of AD mice using *ex vivo* electron microscopy, affecting normal vascular neogenesis and even causing apoptosis, as well as causing some morphological changes in the vessels [3,45], which is consistent with our *in vivo* monitoring results. Notably, compared to WT mice, the percentage of new microvessels and the branching index in AD model mice were lower, despite similar vascular density. Our inference is that AD mice are not in a late stage of pathology, and thus only microangiogenesis is affected. The vascular quantification method is described in the Methods 2.8 and Supplementary Fig. S4. Immuno-histochemically stained brain sections taken by confocal fluorescence microscopy demonstrate an increase in plaque density with age in the hippocampus of mice (Supplementary Fig. S3), confirming the worsening of AD with age (Fig. 6(d)) and illustrating the correlation between the above statistical tendency and the worsening of AD. At the same time, the correlation between the trend of vascular changes and the trend of plaque changes indicates that vascular characteristics are also biomarkers of AD. *In vivo* whole-brain meninges and cortex image could offer comprehensive information for brain disease devotion researches and diagnosis.

4. Conclusion

High-resolution photoacoustic imaging technologies are indispensable tools to accurately quantify brain vasculature architecture, which is important for the study of pathological mechanisms related to blood vessels in the brain. Suffering from balancing tradeoffs among the spatial resolutions as well as the FOV, the brain vasculature architecture of the cerebral and bilateral cortex lost, more or less, in conventional PAMs and PACTs. In this paper, AS-PAM with homogeneous high-resolution was developed for whole-brain meningeal and cortical imaging, taking into account the practical application characteristics and brain shape features. The system provides an arched focal trajectory to match the cylindrical lateral surface of the brain, which contributes to the homogeneous resolution imaging of the mouse cerebral cortex including the lateral brain. We have demonstrated that AS-PAM provides a larger FOV than that of conventional planar-scanning photoacoustic microscope in the mouse cranial maturation process. Moreover, the brains of AD model mice of different ages were imaged and the vascular parameters were quantified. The brain vessel density of both AD model mice and WT mice increased significantly with age, and the branching index of AD mice was not significantly increased, while WT mice showed an increasing trend. The degree of vascular curvature in AD model mice was also lower than that of WT mice, showing a decreasing trend. This funding revealed that the degree of microangio-genesis in AD model is lower than that in WT mice. To the best of our knowledge, this is the first study to observe alterations in the vasculature throughout the soft brain and cortex during the progression of AD *in vivo*. This study also demonstrated that vascular characteristics are a biomarker of AD and reflect the developmental process of AD. In conclusion, AS-PAM has unique whole-brain homogeneous resolution large FOV imaging features that are advantageous for monitoring and assessing function in brain disease progression.

To further optimize the system's ability to detect and quantify neurodegenerative diseases, AS-PAM can be improved in several aspects. First, the system achieves large FOV imaging covering the entire cerebral cortex and maintains homogenous high-resolution imaging, owing to a scanning strategy that matches the brain trajectory. Since the meningeal vascular system is involved in brain feeding and metabolism,

imaging that preserves the meninges allows for comprehensive and reliable information to be obtained. However, the skull has a scattering effect on light. Therefore, longer laser wavelengths were chosen to enhance the depth of the tissue [46]. Second, AS-PAM was designed to solve the problem of out-of-focus images caused by the large height drop difference between the two sides of the brain. It was specially developed for arched sample similar to the brains of small animals. AS-PAM can also be applied to the extremities or backs of small animals, with appropriate animal placement and camber adjustment. Samples with complex shapes may require a more flexible approach, such as a combination of extended focal depth, Z-axis continuously adjustable contour scanning or liquid lens methods [47]. Furthermore, we are enhancing the reconstruction of deep weak signals by establishing a model of light transmission through the skull and tissues through deep learning to obtain better penetration depth for comprehensive imaging of the vasculature in the cortex [48]. If only the vascular changes in the cortex are concerned and imaging deeper blood vessels are imaged, the cranial window schemes and skull transparency schemes are both good solutions [49]. In addition, the morphological and functional alterations in the vasculature, such as blood flow velocity, accompany the AD lesion process [50,51]. AS-PAM could use multiwavelength excitation to perform functional imaging, such as blood oxygen imaging and blood flow velocity detection [52]. The system allows for more whole-brain information and more accurate *in vivo* assessment of the changes in neurovascular features during neurodegenerative disease lesions. Finally, the size of the permanent magnets and coils of the voice coil motor restrict the rotational torque of the motor. However, it is not a principle or insurmountable problem. For large FOV imaging, the scanning speed is limited to 10 Hz to guarantee image quality and prevent image dithering. Real-time imaging could be implemented with a voice coil motor that has a higher torque [53–55]. Employing a laser with a higher repetition frequency allows the sampling rate to be matched to the resolution while the imaging speed is increased. The above experiments demonstrated that the AS-PAM system can achieve homogenous high-resolution imaging of the entire meningeal area while maintaining skull integrity, including the bilateral sides.

AS-PAM system offers the accurate quantization of neurovascular alterations on a while scale. Therefore, we envision several potential applications of AS-PAM in brain disease research of animal models. First, the existing research proved that, in the cortical range, the pathological features of the AD firstly appear in the middle frontal cortex [56]. Based on the system's ability to visualize the neurovascular architecture in the whole cerebral cortex, the relationship between the lesions and the function of each brain region could be explored in future. Second, reduced blood flow has been reported as one of the most consistent physiological deficits in AD [43]. By providing the additional function of blood flow detection, AS-PAM could offer the quantification of vasculature and functional parameters to precisely index the AD regions. In addition, the combination of AS-PAM and blue light photogenetic technology can flexibly intervene the lesion targets in the whole cerebral cortex.

Declaration of Competing Interest

The authors declare that they have no known competing financial interests or personal relationships that could have appeared to influence the work reported in this paper.

Data Availability

Data will be made available on request.

Acknowledgements

Appendix A. Supporting information

Supplementary data associated with this article can be found in the online version at doi:10.1016/j.pacs.2023.100516.

References

[1] C.Y. Santos, P.J. Snyder, W.-C. Wu, M. Zhang, A. Echeverria, J. Alber, Alzheimer's & Dementia: Diagnosis, Assessment & Disease Monitoring 2017, 7 69.
[2] M.D. Sweeney, K. Kisler, A. Montagne, A.W. Toga, B.V. Zlokovic, Nat. Neurosci. 21 (10) (2018) 1318.
[3] M. Nasiriavanaki, J. Xia, H. Wan, A.Q. Bauer, J.P. Culver, L.V. Wang, Proc. Natl. Acad. Sci. 111 (1) (2014) 21.
[4] M.D. Sweeney, A. Montagne, A.P. Sagare, D.A. Nation, L.S. Schneider, H.C. Chui, M.G. Harrington, J. Pa, M. Law, D.J. Wang, Alzheimer's Dement. 15 (1) (2019) 158.
[5] R. Ding, Y. Hase, K.E. Ameen-Ali, M. Ndung'u, W. Stevenson, J. Barsby, R. Gourlay, T. Akinyemi, R. Akinyemi, M.T. Uemura, et al., Brain Pathol. 30 (6) (2020) 1087.
[6] S.L. Warren, A.A. Moustafa, J. Neuroimaging 33 (1) (2023) 5.
[7] S. Lee, R.-E. Yoo, S.H. Choi, S.-H. Oh, S. Ji, J. Lee, K.Y. Huh, J.Y. Lee, I. Hwang, K. M. Kang, Radiology 300 (3) (2021) 661.
[8] J. Ottoy, E. Niemantsverdriet, J. Verhaeghe, E. De Roeck, H. Struyfs, C. Somers, S. Ceyssens, S. Van Mossevelde, T. Van den Bossche, C. Van Broeckhoven, Association of short-term cognitive decline and MCI-to-AD dementia conversion with CSF, MRI, amyloid- and (18)F-FDG-PET imaging, NeuroImage: Clin. 22 (2019), 101771.
[9] S. Vandenberghe, P. Moskal, J.S. Karp, EJNMMI Phys. 7 (2020) 1.
[10] P. Rajiah, A. Parakh, F. Kay, D. Baruah, A.R. Kambadakone, S. Leng, Radiographics 40 (5) (2020) 1284.
[11] M. Kislin, J. Sword, I.V. Fomitcheva, D. Croom, E. Pryazhnikov, E. Lihavainen, D. Toptunov, H. Rauvala, A.S. Ribeiro, L. Khiroug, J. Neurosci. 37 (2) (2017) 333.
[12] M. Clough, I.A. Chen, S.-W. Park, A.M. Ahrens, J.N. Stirman, S.L. Smith, J.L. Chen, Nat. Commun. 12 (1) (2021) 6638.
[13] S. Gottschalk, O. Degtyaruk, B. Mc Larney, J. Rebling, M.A. Hutter, X.L. De ́an-Ben, S. Shoham, D. Razansky, Nat. Biomed. Eng. 3 (5) (2019) 392.
[14] M. Omar, J. Aguirre, V. Ntziachristos, Nat. Biomed. Eng. 3 (5) (2019) 354.
[15] R. Gao, Z. Xu, Y. Ren, L. Song, C. Liu, Photoacoustics 22 (2021), 100243.
[16] C. Liu, J. Chen, Y. Zhang, J. Zhu, L. Wang, Adv. Photonics 3 (1) (2021), 016002.
[17] S. Cheng, Y. Zhou, J. Chen, H. Li, L. Wang, P. Lai, Photoacoustics 25 (2022), 100314.
[18] J.W. Baik, H. Kim, M. Son, J. Choi, K.G. Kim, J.H. Baek, Y.H. Park, J. An, H.Y. Choi, S.Y. Ryu, Laser Photonics Rev. 15 (10) (2021), 2100124.
[19] X. Zhu, Q. Huang, A. DiSpirito, T. Vu, Q. Rong, X. Peng, H. Sheng, X. Shen, Q. Zhou, L. Jiang, Light.: Sci. Appl. 11 (1) (2022) 138.
[20] T. Jin, W. Qi, X. Liang, H. Guo, Q. Liu, L. Xi, Laser Photonics Rev. 16 (2) (2022), 2100304.
[21] J.W. Baik, J.Y. Kim, S. Cho, S. Choi, J. Kim, C. Kim, IEEE Trans. Med. Imaging 39 (4) (2019) 975.
[22] J. Chen, Y. Zhang, L. He, Y. Liang, L. Wang, Photoacoustics 20 (2020), 100195.
[23] M. Chen, L. Jiang, C. Cook, Y. Zeng, T. Vu, R. Chen, G. Lu, W. Yang, U. Hoffmann, Q. Zhou, Photoacoustics 28 (2022), 100417.
[24] J. Kim, J.Y. Kim, S. Jeon, J.W. Baik, S.H. Cho, C. Kim, Light: Science & Applications 8 (1) (2019) 103.
[25] M. Chen, X. Duan, B. Lan, T. Vu, X. Zhu, Q. Rong, W. Yang, U. Hoffmann, J. Zou, J. Yao, Photoacoustics 24 (2021), 100309.
[26] C. Zhang, H. Zhao, S. Xu, N. Chen, K. Li, X. Jiang, L. Liu, Z. Liu, L. Wang, K. K. Wong, Opt. Lett. 45 (15) (2020) 4312.
[27] B.-O. Guan, L. Jin, J. Ma, Y. Liang, X. Bai, Opto-Electron. Adv. 4 (8) (2021), 200081.
[28] C. Yeh, B. Soetikno, S. Hu, K.I. Maslov, L.V. Wang, J. biophotonics 8 (4) (2015) 303.
[29] Z. Xu, Y. Pan, N. Chen, S. Zeng, L. Liu, R. Gao, J. Zhang, C. Fang, L. Song, C. Liu, Photoacoustics 26 (2022), 100342.
[30] B. Park, H. Lee, S. Jeon, J. Ahn, H.H. Kim, C. Kim, J. biophotonics 12 (2) (2019), e201800215.
[31] Y. Zhou, N. Sun, S. Hu, IEEE Trans. Med. Imaging 41 (12) (2022) 3544–3551.
[32] R. Gao, Q. Xue, Y. Ren, H. Zhang, L. Song, C. Liu, Photoacoustics 26 (2022), 100328.
[33] R. Cao, J. Zhao, L. Li, L. Du, Y. Zhang, Y. Luo, L. Ming, S. Davis, Q. Zhou, A. Zerad, L.V. Wang, Nat. Photonics 17 (1) (2023) 89–95.
[34] Z. Xu, N. Sun, R. Cao, Z. Li, Q. Liu, S. Hu, Neurophotonics 6 (3) (2019), 035012.
[35] Y. Wang, F. Zhong, N. Sun, Z. Xu, J. Li, Q. Liu, Z. Li, Z. Zuo, S. Hu, Opt. Lett. 47 (8) (2022) 1988.
[36] T.T. Mai, S.W. Yoo, S. Park, J.Y. Kim, K.-H. Choi, C. Kim, S.Y. Kwon, J.-J. Min, C. Lee, Sensors 21 (5) (2021) 1776.
[37] M.M. Khansari, Ph.D. thesis, University of Illinois at Chicago, 2017.
[38] M.M. Khansari, S.L. Garvey, S. Farzad, Y. Shi, M. Shahidi, Int. J. Retin. Vitr. 5 (2019) 1.
[39] M.M. Khansari, W. O'Neill, J. Lim, M. Shahidi, Biomed. Opt. Express 8 (8) (2017) 3796.
[40] B. Xiong, A. Li, Y. Lou, S. Chen, B. Long, J. Peng, Z. Yang, T. Xu, X. Yang, X. Li, T. Jiang, Q. Luo, H. Gong, Front. Neuroanat. 11 (2017) 128.
[41] Q. Wang, S.-L. Ding, Y. Li, J. Royall, D. Feng, P. Lesnar, N. Graddis, M. Naeemi, B. Facer, A. Ho, Cell 181 (4) (2020) 936.
[42] S. Dutta, P. Sengupta, Life Sci. 152 (2016) 244.
[43] E.P. Meyer, A. Ulmann-Schuler, M. Staufenbiel, Proc. Natl. Acad. Sci. 105 (9) (2008) 3587–3592.
[44] E. Zudaire, L. Gambardella, C. Kurcz, S. Vermeren, PLoS One 6 (11) (2011), e27385.
[45] D. Boche, E. Zotova, R. Weller, S. Love, J.W. Neal, R. Pickering, D. Wilkinson, C. Holmes, J. Nicoll, Brain 131 (12) (2008) 3299.
[46] J. Shi, T.T. Wong, Y. He, L. Li, R. Zhang, C.S. Yung, J. Hwang, K. Maslov, Wang, L. V, Nat. Photonics 13 (9) (2019) 609–615.
[47] K. Xiong, S. Yang, X. Li, D. Xing, Opt. Lett. 43 (8) (2018) 1846–1849.
[48] H. Zhao, Z. Ke, F. Yang, K. Li, N. Chen, L. Song, C. Zheng, C. Liu, Adv. Sci. 8 (3) (2021), 2003097.
[49] Y. Wang, G. Liang, F. Liu, Q. Chen, L. Xi, IEEE Trans. Biomed. Eng. 68 (2) (2020) 706–711.
[50] W. Qin, Q. Gan, L. Yang, Y. Wang, W. Qi, B. Ke, L. Xi, NeuroImage 238 (2021), 118260.
[51] W. Zhang, H. Ma, Z. Cheng, Z. Wang, K. Xiong, S. Yang, Opt. Lett. 45 (7) (2020) 1599.
[52] R. Cao, J. Li, B. Ning, N. Sun a, T. Wanga, Z. Zuo, S. Hu, Neuroimage 150 (2017) 77–87.
[53] R. Ni, Z. Chen, X.L. De ́an-Ben, F.F. Voigt, D. Kirschenbaum, G. Shi, A. Villois, Q. Zhou, A. Crimi, P. Arosio, Nat. Biomed. Eng. 6 (9) (2022) 1031.
[54] J. Chen, Y. Zhang, X. Li, J. Zhu, D. Li, S. Li, C.-S. Lee, L. Wang, Photonics Res. 8 (12) (2020) 1875.
[55] A.B.E. Attia, G. Balasundaram, M. Moothanchery, U. Dinish, R. Bi, V. Ntziachristos, M. Olivo, Photoacoustics 16 (2019), 100144.
[56] M. Kulijewicz-Nawrot, A. Verkhratsky, A. Chvatal, E. Sykova, J.J. Rodríguez, J. Anat. 221 (3) (2012) 252–262.

Ting Guo She received her master's degree from South China Normal University in 2021. She joined the South China University of Technology in September 2021. Her research focuses on the development and applications of Photoacoustic microscopy and brain imaging.

Kedi Xiong Associate researcher, South China Normal University. He received his PhD in optics from South China Normal University in 2018. Long-term commitment to photoacoustic imaging methods, systems and application research, around clinical diseases and application transformation, launched a comprehensive, in-depth system development research.

Bo Yuan He received his bachelor's degree from Hubei Second Normal University in 2021. He is mainly engaged in the research and development of ultrasonic transducers.

Yuhu Zhang A professor at Guangdong General Hospital. He is mainly engaged in clinical and research work on Parkinson's disease, movement disorders, and neurogenetic diseases.

Zhenhui Zhang He received his PhD in optics from South China Normal University in 2018. The research content includes photoacoustic imaging theory, super-resolution imaging and polarization imaging technology.

Changhong Liang A professor at Guangdong General Hospital, He is the Chief scientist of the National key Research and Development Program and the leading medical talent of Guangdong Province. His research focuses on imaging diagnosis of abdominal diseases and cardiovascular diseases.

Lijuan Wang A professor at Guangdong General Hospital. She focuses on the clinical diagnosis and treatment of Parkinson's disease, cerebrovascular disease, memory disorders and other directions.
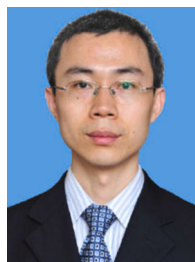
Zaiyi Liu A professor at Guangdong General Hospital. He received his PhD from West China Hospital, Sichuan University in 2004. He is committed to the cross-research of medicine and industry, aiming at the clinical challenge of the lack of quantitative means in conventional image analysis, mining medical image big data information, and building intelligent prediction models to assist clinical decision-making.